



A peridynamic model for contact problems involving fracture

Heng Zhang, Xiong Zhang^{*}, Yan Liu

School of Aerospace Engineering, Tsinghua University, Beijing 100084, China

ARTICLE INFO

Keywords:

Peridynamics
Contact model
Frictional crack
Node to region

ABSTRACT

A new nonlocal peridynamic contact model is proposed for contact problems accompanied with crack growth. Two long-range peridynamic contact bond forces are developed to study the sticking and sliding frictional contact. A numerical algorithm is proposed to determine the contact surface normal vector and contact condition. Three numerical examples, including contact of two elastic plates, the end loaded split specimens with frictional interface cracks and Kalthoff-Winkler contact tests, are successively investigated to verify and validate the model. Numerical results are compared with the available analytical, finite element method (FEM) and experimental solutions, which demonstrates that the proposed peridynamic contact model can successfully capture both the contact and fracture behaviors.

1. Introduction

Contact problems are ubiquitous in natural and engineer systems and are often accompanied by material and structural failures, such as impact fracture and frictional crack growth. Therefore, contact problems involving materials fracture need to be investigated for both contact and fracture behaviors prediction.

The analytical contact solutions were developed for deformation, stress and pressure predictions based on the Hertz contact [1], and crack surface contact [2,3] models, but they can only be applied in some ideal situation. The numerical method, like finite element method (FEM) has been widely utilized for the contact problems [4–6], and achieved great success in contact response predictions. However, the original FEM meets great challenge due to its inadequacy in dealing with discontinuity when the fracture behaviors are considered in the contact problems. The material point method (MPM) [7] and smoothed particle hydrodynamics (SPH) [8,9] have been successfully applied in the impact and penetration contact simulations, but further study is still needed to investigate the material fracture behavior associated with contact.

Peridynamics (PD), as a nonlocal reformulation of continuous mechanics, was proposed by Silling in 2000 [10] for discontinuous problems analysis. In PD theory, spatial derivatives are not needed, and the partial-differential governing equations in continuous mechanics are replaced by the integral-differential equations. Therefore, the PD model can be naturally utilized for the discontinuous problems, such as the crack initiation, propagation and path selection, without any special techniques. The original version of peridynamics was first proposed as the bond-based peridynamic (BB-PD) model, which assumes that any two points within the horizon are connected with a bond through spring-like interaction. However, this assumption leads to material parameters restrictions in BB-PD model [11]. The state-based peridynamics (SB-PD) [12] was then proposed as a more general frame, in which the bond force density of the peridynamic point depends on its whole family deformation. Meanwhile, various bond failure models in peridynamics have been proposed for quantitatively fracture analysis, such as the critical stretch-based criterion [11,13], critical energy density-based criterion

^{*} Corresponding author.

E-mail addresses: hengzh@tsinghua.edu.cn (H. Zhang), xzhang@tsinghua.edu.cn (X. Zhang).

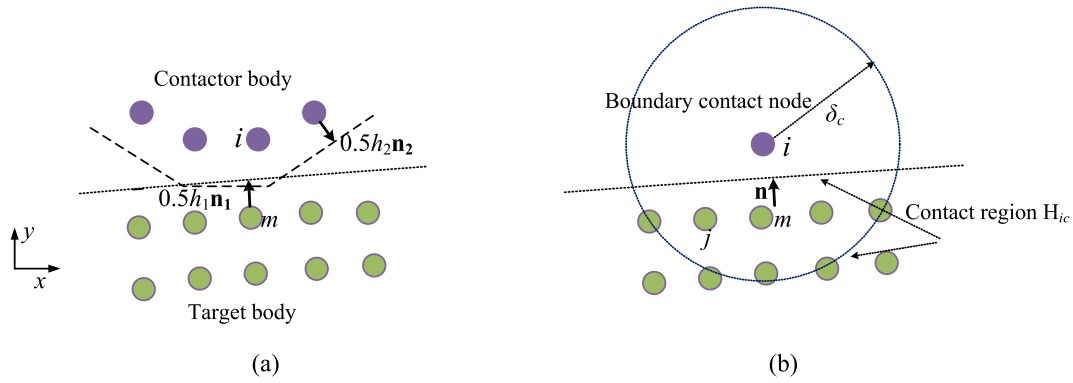


Fig. 1. Discrete peridynamic models in the contact region: (a) nonlocal contact between two peridynamic models, and (b) boundary contact node x_i in contact with its contact region H_{ic} .

[14], mixed-mode bond failure criterion [15], and strength and energy coupled failure model [16–18]. Additionally, classical fracture mechanic methods have also been reformulated in the framework of peridynamic theory, for example, the J-integral [19,20], virtual crack closure technique [21,22], and cohesive zone model [23–25].

With the capability of handling discontinuities, the peridynamic theory has been successfully utilized in the failure predictions of various problems, such as dynamic brittle fracture [26–28], failure of composite materials [29–31] and crack growth in rocks and concretes [32–37]. Meanwhile, it was also applied for the contact problems. The original peridynamic contact model was proposed by Macek and Silling [38] with definition of the short-range contact force, which was later utilized for dynamic contact problems [39,40]. The impact contact model considering deformable target and rigid or flexible impactor was presented by Madenci and Oterkus [41], and was extended for impact contact analysis [34,42]. Additionally, the fracture problems associated with contact were analyzed in peridynamics with the penalty contact model [43], peridynamic and FEM contact model [44], frictional contact model [45] and interface nonlocal contact model [46,47]. However, in above studies, there is no peridynamic contact model considering both sticking and frictional contact, and the contact condition has not been well evaluated.

In this paper, a nonlocal peridynamic contact model is proposed for the contact and fracture problems analysis. First, peridynamic contact bonds are defined for the nonlocal contact modeling, and two long-range contact bond forces are developed to study the sticking and sliding frictional contact. A numerical algorithm is proposed to determine the contact surface normal vector and contact condition. Three examples, including contact of two elastic plates, the end loaded split specimens with frictional interface cracks and Kalthoff-Winkler contact tests, are studied to verify the proposed model. The contact and fracture behaviors (e.g. contact force, crack path and crack velocity) are predicted by the proposed contact model, the obtained results agree well with those from the analytical solution, finite element method (FEM) and experiments.

2. Nonlocal peridynamic contact model

In this section, a new nonlocal version of peridynamic contact model is proposed, in which peridynamic contact bonds are defined for the nonlocal contact modeling, and two long-range contact bond forces are developed to study sticking and sliding frictional contact.

2.1. Formation of the contact between peridynamic models

The contact region of two discrete peridynamic models, considered as the contactor and target, is shown in Fig. 1(a). In the peridynamic numerical models, the boundary surfaces of the target and contactor are artificially obtained with the extension of $0.5 h_1$ and $0.5 h_2$ from the outermost nodes along their outward unit normal vectors \mathbf{n}_1 and \mathbf{n}_2 , where h_1 and h_2 are the grid sizes of the peridynamic target and contactor bodies. Since the basic contact condition is that no material overlap can occur, the contact in peridynamic models happens when:

$$(\mathbf{y}_i - \mathbf{y}_m) \cdot \mathbf{n} < 0.5(h_1 + h_2), \quad \text{and} \quad |\mathbf{y}_i - \mathbf{y}_m| < \frac{\sqrt{2}}{2}(h_1 + h_2) \quad (1)$$

where \mathbf{y}_i and \mathbf{y}_m are the deformed vectors of boundary nodes \mathbf{x}_i and \mathbf{x}_m , in which \mathbf{x}_i and \mathbf{x}_m are the outermost nodes belong to contactor and target bodies, respectively, and \mathbf{n} is the unit normal vector of the contact surface.

When Eq. (1) is satisfied, as shown in Fig. 1(b), the boundary node \mathbf{x}_i is thus in contact with its contact region H_{ic} , where the contact horizon δ_c is defined, \mathbf{x}_j is the node in H_{ic} that belongs to target body. Simultaneously, the boundary node \mathbf{x}_m in target body is in contact with its contact region H_{mc} , which belongs to contactor body. Therefore, even though the contact condition of Eq. (1) is defined locally with the boundary nodes, the contact is realized in the nonlocal form with their contact regions. Additionally, there is no real constructed contact surface in the peridynamic contact region, and the normal vector \mathbf{n} can be obtained by the normal vectors of relative

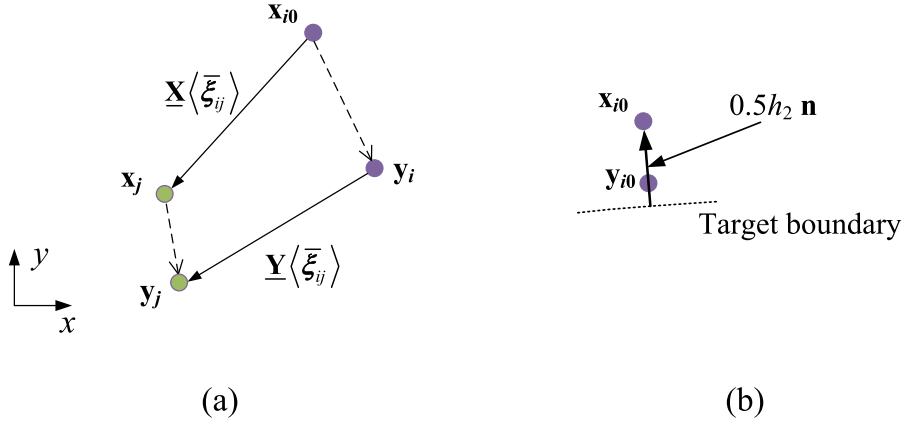


Fig. 2. The peridynamic contact setup: (a) the peridynamic contact bond (between node x_i and its contact node x_j), and (b) the reference location of the node x_i from the deformed location y_{i0} .

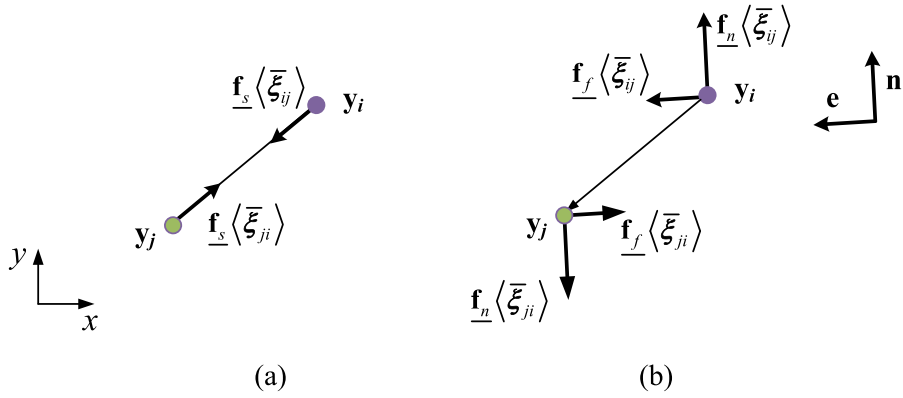


Fig. 3. The peridynamic contact bond forces in the conditions of (a) sticking and (b) sliding frictional contact.

contact nodes, which is presented in the following section.

The connection between boundary contact node and its contact nodes can be called as the peridynamic contact bond $\bar{\xi}$, in which the overline mark is used for distinguishing to the original peridynamic bond. As shown in Fig. 2(a), the contact bond $\bar{\xi}_{ij} = x_j - x_i$ is defined, and $\underline{X}\langle \bar{\xi}_{ij} \rangle$ and $\underline{Y}\langle \bar{\xi}_{ij} \rangle$ are its reference and deformed vectors. The reference location of boundary node x_i before contact is marked as x_{i0} , which can be relocated by its deformed location in the initial contact step y_{i0} , as $0.5 h_2$ distance from the target boundary along its normal vector (see Fig. 2(b)). When the contact happens, the contact bond $\bar{\xi}_{ij}$ deforms from $\underline{X}\langle \bar{\xi}_{ij} \rangle$ to $\underline{Y}\langle \bar{\xi}_{ij} \rangle$, and two kinds of deformed states are defined as:

$$s\langle \bar{\xi}_{ij} \rangle = \frac{|\underline{Y}\langle \bar{\xi}_{ij} \rangle| - |\underline{X}\langle \bar{\xi}_{ij} \rangle|}{|\underline{X}\langle \bar{\xi}_{ij} \rangle|}, \quad s_n\langle \bar{\xi}_{ij} \rangle = \frac{|\underline{Y}\langle \bar{\xi}_{ij} \rangle \cdot \mathbf{n}| - |\underline{X}\langle \bar{\xi}_{ij} \rangle \cdot \mathbf{n}|}{|\underline{X}\langle \bar{\xi}_{ij} \rangle \cdot \mathbf{n}|} \quad (2)$$

where s and s_n are the bond stretch and the bond normal stretch, respectively, and it is easy to know that these values are negative due to contact.

2.2. Peridynamic contact bond forces

In this nonlocal formulation contact, two formations of peridynamic contact bond force are defined for two different contact cases (see Fig. 3). In the sticking contact, the peridynamic sticking contact bond force is defined as:

$$\mathbf{f}_s\langle \bar{\xi}_{ij} \rangle = c_s s\langle \bar{\xi}_{ij} \rangle \omega\langle \bar{\xi}_{ij} \rangle \frac{\underline{Y}\langle \bar{\xi}_{ij} \rangle}{|\underline{Y}\langle \bar{\xi}_{ij} \rangle|} \quad (3)$$

While in the sliding frictional contact, the peridynamic normal and tangential contact bond forces can be respectively expressed as:

$$\underline{\mathbf{f}}_n\langle\bar{\xi}_{ij}\rangle = -c_n s_n \langle\bar{\xi}_{ij}\rangle \omega\langle\bar{\xi}_{ij}\rangle \mathbf{n} \quad (4)$$

$$\underline{\mathbf{f}}_f\langle\bar{\xi}_{ij}\rangle = \mu \left| \underline{\mathbf{f}}_n\langle\bar{\xi}_{ij}\rangle \right| \mathbf{e} \quad (5)$$

where \underline{s} and s_n are the bond stretch and the bond normal stretch in Eq. (2), ω is the influence function, μ is the frictional coefficient, \mathbf{n} and \mathbf{e} are the unit normal and tangential vectors of the contact surface, where \mathbf{e} is inversed to the sliding direction. c_s and c_n are the sticking and sliding micromodulus for the peridynamic contact bond, and in the two-dimensional (2D) case, they can be expressed as:

$$c_s = \beta_s \frac{3E_c}{4\delta_c^2 B h_2}; \quad c_n = \beta_n \frac{E_c}{4\delta_c^2 B h_2} \quad (6)$$

where δ_c is the contact horizon (see Fig. 1(b)), B is the thickness of 2D model, h_2 is the grid size of the peridynamic contactor model, β_s and β_n are the modified coefficients, and E_c is contact stiffness that takes the form of:

$$\frac{2}{E_c} = \frac{1 - \nu_1^2}{E_1} + \frac{1 - \nu_2^2}{E_2} \quad (7)$$

where E_1 and E_2 are the elastic modulus, ν_1 and ν_2 are the Poisson's ratios of the contactor and target. The detail of derivative process for Eq. (6) is shown in Appendix.

Overall, the formations of peridynamic contact bond force are different for the sticking and sliding contact. As presented in Eq. (3), the sticking contact bond can be regarded as the original peridynamic compressive bond, since the bond stretch \underline{s} is utilized for bond force computation and the force direction is along its deformed vector. While in the sliding frictional contact, the bond normal stretch s_n is calculated and the tangential component of bond deformation has no contribution to contact bond forces. Additionally, for both sticking and sliding cases, the contact bond forces are restricted by the Newton's Third law as:

$$\underline{\mathbf{f}}\langle\bar{\xi}_{ij}\rangle = -\underline{\mathbf{f}}\langle\bar{\xi}_{ji}\rangle \quad (8)$$

Which provides the bond force formations of contact region nodes, and also ensures the linear admissibility condition.

2.3. Peridynamic contact force density

For the boundary node \mathbf{x}_i in contact (see Fig. 1), its peridynamic contact force density can be expressed as:

$$\mathbf{F}_i = \sum_{j \in H_{ic}} \underline{\mathbf{f}}\langle\bar{\xi}_{ij}\rangle dV_j - \sum_{j \in B_{ic}} \underline{\mathbf{f}}\langle-\bar{\xi}_{ij}\rangle dV_j \quad (9)$$

where $\underline{\mathbf{f}}$ is the peridynamic contact bond force given in Eqs. (3)–(5), H_{ic} is the contact region in Fig. 1(b), B_{ic} is the boundary region whose contact regions include node \mathbf{x}_i . Thus, the total contact force \mathbf{F}_i of boundary contact node contains two parts, the first part is related to its contact region H_{ic} and the other part is from the boundary region B_{ic} whose contact regions include node \mathbf{x}_i .

While if contact involving node \mathbf{x}_i is not the boundary contact node, the first part of contact force in Eq. (9) is equal to 0, and the contact force density can be reduced as:

$$\mathbf{F}_i = - \sum_{j \in B_{ic}} \underline{\mathbf{f}}\langle-\bar{\xi}_{ij}\rangle dV_j \quad (10)$$

Which shows \mathbf{F}_i is only from its corresponding boundary contact region B_{ic} , where the contact bond force can be computed by Eq. (8).

3. Implementation of the peridynamic contact model

In the peridynamic numerical model with contact, the motion equation of peridynamic node \mathbf{x}_i can be expressed as:

$$\rho_i \ddot{\mathbf{u}}_i(\mathbf{x}_i, t) = \sum_{k \in H_i} \left\{ \mathbf{T}[\mathbf{x}_i, t]\langle\bar{\xi}_{ik}\rangle - \mathbf{T}[\mathbf{x}_k, t]\langle-\bar{\xi}_{ik}\rangle \right\} dV_j + \mathbf{F}_i + \mathbf{b}_i(\mathbf{x}_i, t) \quad (11)$$

where ρ_i is the density of node \mathbf{x}_i , \mathbf{u}_i is its displacement at time t , H_i is the neighborhood horizon of \mathbf{x}_i , \mathbf{x}_k is the neighbor node in H_i that satisfies $|\mathbf{x}_k - \mathbf{x}_i| < \delta$, δ is the peridynamic horizon size, $\bar{\xi}_{ik} = \mathbf{x}_k - \mathbf{x}_i$ is the bond vector, $\mathbf{T}[\mathbf{x}_i, t]$ and $\mathbf{T}[\mathbf{x}_k, t]$ are the force vector states of nodes \mathbf{x}_i and \mathbf{x}_k , respectively. \mathbf{F}_i is the contact force density in Eq. (9), $\mathbf{b}_i(\mathbf{x}_i, t)$ is the body force density. In this study, the uniform grid size Δx is utilized for both target and contactor models, which leads to $h_1 = h_2 = \Delta x$, and horizon size $\delta = m\Delta x$ is considered. Additionally, it is easy to know that there is no overlapped region between the neighborhood H_i and contact region H_{ic} , since they belong to different bodies.

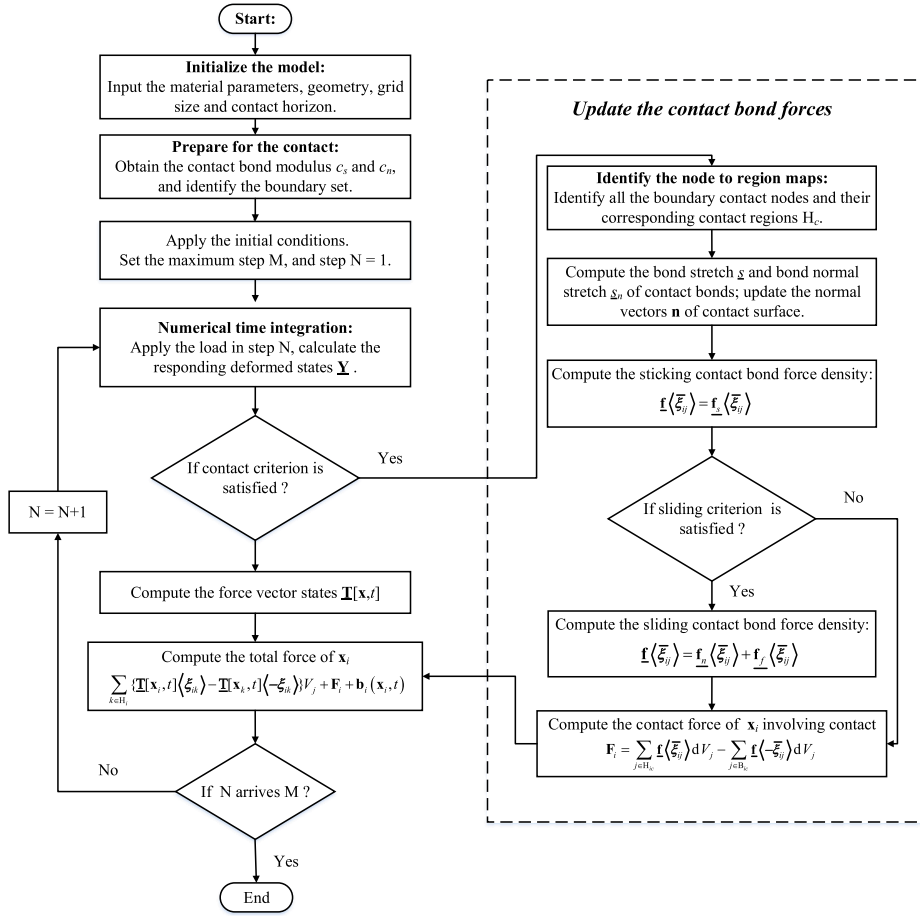


Fig. 4. The flowchart of the nonlocal peridynamic contact model.

3.1. Normal vectors of the contact surface

The normal vector of the contact surface is essential for the contact condition evaluation and contact force computation. Here, the normal vectors of contact boundary nodes are calculated for their corresponding contact surface normal vector computation.

The weighted mass of the peridynamic node \mathbf{x}_i in the deformed state is defined as:

$$q_i = \rho_i \underline{y} \cdot \underline{y} = \sum_{m \in H_i} \rho_i \langle \underline{y} \underline{y} \rangle \langle \xi_{im} \rangle V_m \quad (12)$$

where ρ_i is the density of node \mathbf{x}_i , \underline{y} is the deformation scalar state computed as $[\underline{Y}]$. The unit outward normal vector of node \mathbf{x}_i can be obtained by the gradient of its weighted mass as:

$$\mathbf{n}_i = -\frac{q_{i,I}}{|q_{i,I}|} = -\frac{\sum_{m \in H_i} \rho_i \langle \underline{y} \underline{y} \rangle \langle \xi_{im} \rangle_{,I} V_m}{\left| \sum_{m \in H_i} \rho_i \langle \underline{y} \underline{y} \rangle \langle \xi_{im} \rangle_{,I} V_m \right|} = -\frac{\sum_{m \in H_i} (y_{mI} - y_{iI}) V_m}{\left| \sum_{m \in H_i} (y_{mI} - y_{iI}) V_m \right|} \quad (13)$$

where $q_{i,I}$ means the partial derivative of q_i in the I direction, and y_{mI} means the I directional component of the deformed vector \mathbf{y}_m . The derivation detail of Eq. (13) is given in Appendix.

In the peridynamic contact region, the unit outward normal vectors in the target and contactor are called as \mathbf{n}_1 and \mathbf{n}_2 , respectively (see Fig. 1 (a)). Thus, for a node to region contact map (see Fig. 1 (b)), the normal vector of the node \mathbf{x}_i is \mathbf{n}_{2i} ; while the normal vector of its contact region is defined as the average value of all the normal vectors of contained nodes as:

$$\bar{\mathbf{n}}_1 = \frac{\sum_M \mathbf{n}_{1j}}{\left| \sum_M \mathbf{n}_{1j} \right|} \quad (14)$$

where M is the total number of the nodes in the contact region. However, the collinearity condition may not be satisfied between

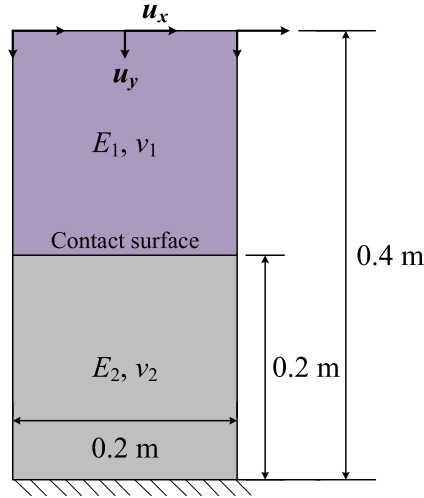


Fig. 5. Contact test of two plates with different materials.

normal vectors \mathbf{n}_{2i} and $\bar{\mathbf{n}}_1$, and the modified normal vector is thus defined at the contact surface as:

$$\mathbf{n} = \frac{\bar{\mathbf{n}}_1 - \mathbf{n}_{2i}}{|\bar{\mathbf{n}}_1 - \mathbf{n}_{2i}|} \quad (15)$$

3.2. Evaluation of contact conditions

Evaluation of contact conditions is fundamental for solving contact problems, with which the suitable formations of peridynamic bond force can be applied. In other words, the criteria should be defined for whether a peridynamic node is in contact and which kinds of contact, sticking or sliding contact, is ongoing.

The contact criterion is given in Eq. (1). When Eq. (1) is satisfied, the sticking contact is firstly considered, and the peridynamic bond force for contact bond $\bar{\xi}_{ij}$ would be applied as:

$$\underline{\mathbf{f}}\langle\bar{\xi}_{ij}\rangle = \underline{\mathbf{f}}_s\langle\bar{\xi}_{ij}\rangle \quad (16)$$

When the peridynamic force of the node \mathbf{x}_i satisfies the criterion of:

$$\left| \sum_{j \in H_{ic}} \underline{\mathbf{f}}_s\langle\bar{\xi}_{ij}\rangle \cdot \mathbf{e} dV_j \right| \mu \left| \sum_{j \in H_{ic}} \underline{\mathbf{f}}_s\langle\bar{\xi}_{ij}\rangle \cdot \mathbf{n} dV_j \right| \quad (17)$$

The contact is changed from sticking to sliding frictional condition, and the peridynamic contact bond force is changed into:

$$\underline{\mathbf{f}}\langle\bar{\xi}_{ij}\rangle = \underline{\mathbf{f}}_n\langle\bar{\xi}_{ij}\rangle + \underline{\mathbf{f}}_t\langle\bar{\xi}_{ij}\rangle \quad (18)$$

In addition, the contact should be released when the direction of normal contact force is inverted as:

$$\sum_{j \in H_{ic}} \underline{\mathbf{f}}_n\langle\bar{\xi}_{ij}\rangle \cdot \mathbf{n} dV_j < 0 \quad (19)$$

Then, the normal and tangential peridynamic contact bond forces are all set to zero when the contact is released.

Therefore, using the criteria of Eqs. (1), (17) and (19), the contact conditions of sticking, sliding and release are all evaluated, and the whole contact process can be captured. While if the sliding frictional contact is individually considered, the peridynamic sliding contact bond force in Eq. (18) is directly applied without the sliding evaluation of Eq. (17).

3.3. Flowchart of the peridynamic contact model

In general, the whole process of the proposed nonlocal peridynamic contact model is presented in Fig. 4.

As shown in Fig. 4, the node sets near the boundary are identified for contact evaluation preparation. In each time step, when the contact criterion in Eq. (1) is satisfied, the bond stretch and bond normal stretch of contact bonds are calculated by Eq. (2), and the normal vectors of contact surface are computed by Eq. (15). The contact bond forces are then obtained and applied by Eqs. (16) and (18) for sticking and sliding frictional contact, while the contact conditions are evaluated in Eq. (17).

Overall, the nonlocal version of peridynamic contact model is established. Unlike to the original node to node short-range contact models, the contact force acts over the volumetric region rather than the single node; the normal vector of the contact surface is

Table 1
Material properties of two plates.

Material	E (GPa)	ν	ρ (kg/m ³)
1	200	0.27	7850
2	100	0.27	7850

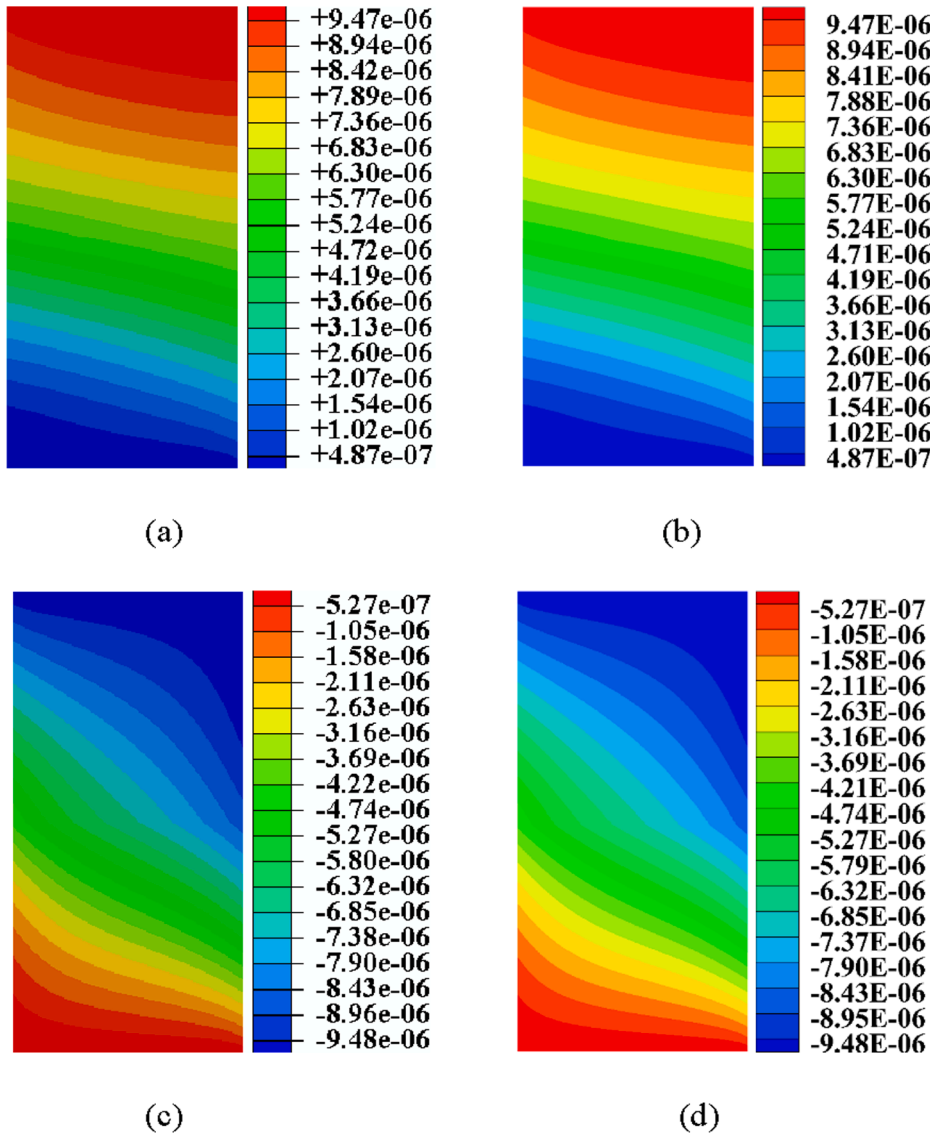


Fig. 6. Comparisons of displacement distributions in x-direction: (a) FEM and (b) Peridynamics, and y-direction: (c) FEM and (d) peridynamics, when $u_x = 1.0 \times 10^{-5}$ m (sticking friction).

calculated and the sticking and frictional sliding contact can all be captured. Meanwhile, if the contact horizon $\delta_c \leq \sqrt{2}\Delta x$ is considered, the contact region would contain only one single node, and this node to region contact model is reduced into the node to node version. In which the sticking contact cannot be correctly modeled, since the direction of the contact force is strongly affected by the grid strategy and contact location. However, if the sliding frictional contact problem is individually considered, this reduced node to node version contact model can still be applied.

4. Examples

In this section, three examples, including contact of two elastic plates, the end loaded split (ELS) with frictional interface crack and

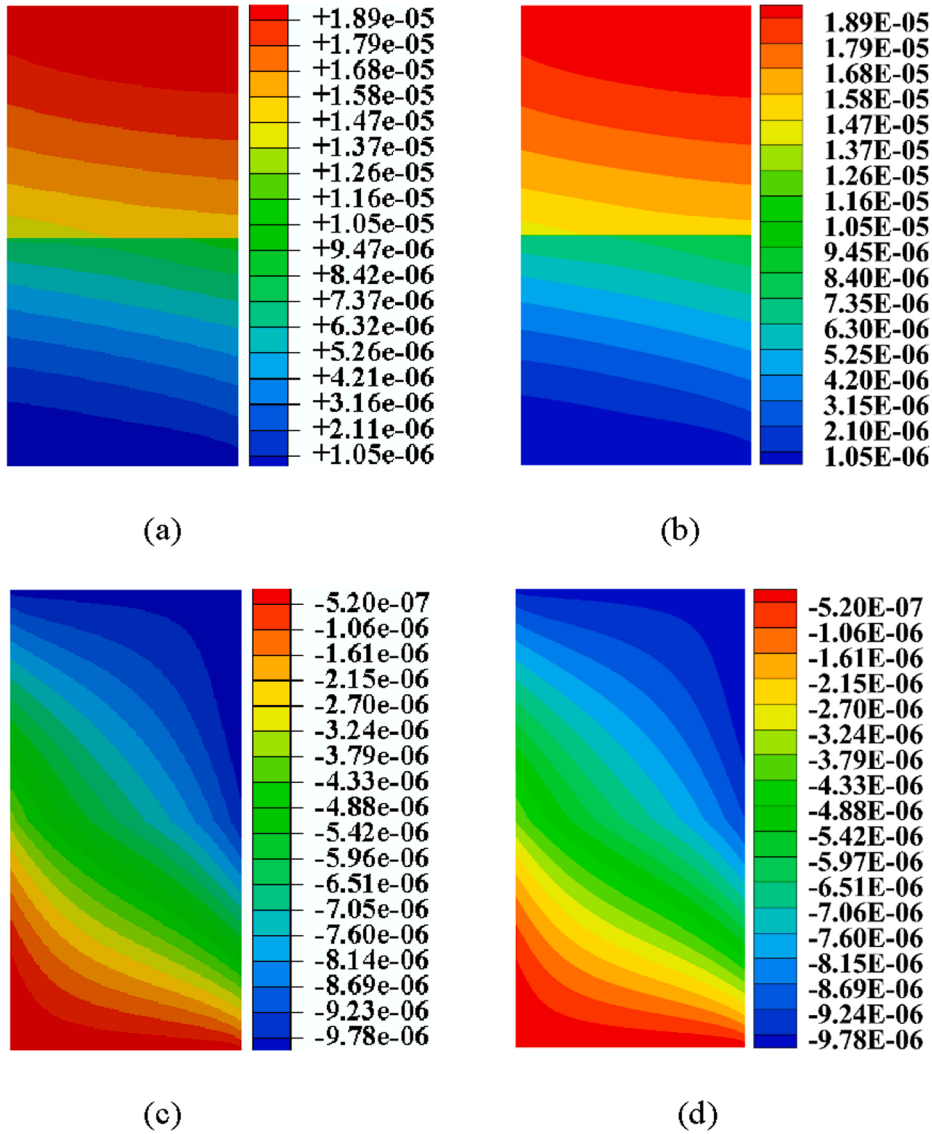


Fig. 7. Comparisons of displacement distributions in x-direction: (a) FEM and (b) Peridynamics, and y-direction: (c) FEM and (d) peridynamics, when $u_x = 2.0 \times 10^{-5}$ m (sliding friction).

Kalthoff-Winkler (KW) tests, are analyzed by the proposed peridynamic contact model to verify and validate the model.

4.1. Contact of two plates

4.1.1. Frictional contact of two plates

First, the contact of two elastic plates is investigated. The geometrical sizes and boundary conditions of the two plates are shown in Fig. 5. Different elastic materials are utilized for two plates, and the material properties are given in Table 1. The plane stress condition is considered, and the uniform thickness of $B = 1$ mm is used. The frictional contact is investigated with the fixed compressive displacement load of $u_y = -1.0 \times 10^{-5}$ m and different sliding displacement loads of $u_x = 1.0 \times 10^{-5}$ m and 2.0×10^{-5} m. The frictional coefficient value of $\mu = 0.2$ is used.

In peridynamic numerical model, the δ -convergence study [48] is performed with the decreasing horizon values of $\delta = 16$ mm, 8 mm and 4 mm, and the fixed value of $m = 4$. The adaptive dynamic relaxation (ADR) [49] method is utilized to get the final stable solution. For peridynamic contact analysis, the proposed peridynamic contact model in Fig. 4 is performed in which the contact horizon is equal to nonlocal horizon as $\delta_c = \delta$. The finite element method (FEM) is also used for the results comparison.

The displacement distributions of two plates with frictional contact are presented in Figs. 6 and 7, in which the fixed values of $\delta = 4$ mm and $m = 4$ are used. Meanwhile, for the quantitative comparison, the displacement components along the y-axis are typically

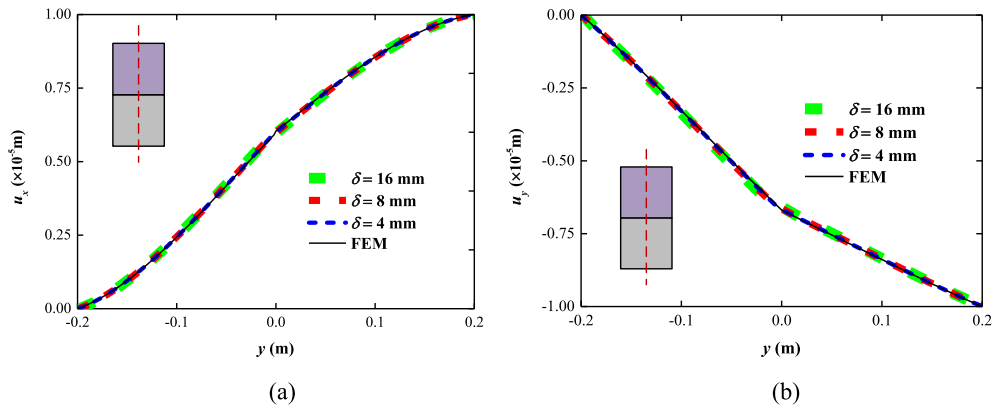


Fig. 8. Displacement distributions along the middle line in x-direction (a) and y-direction (b), when $u_x = 1.0 \times 10^{-5}$ m (sticking friction).

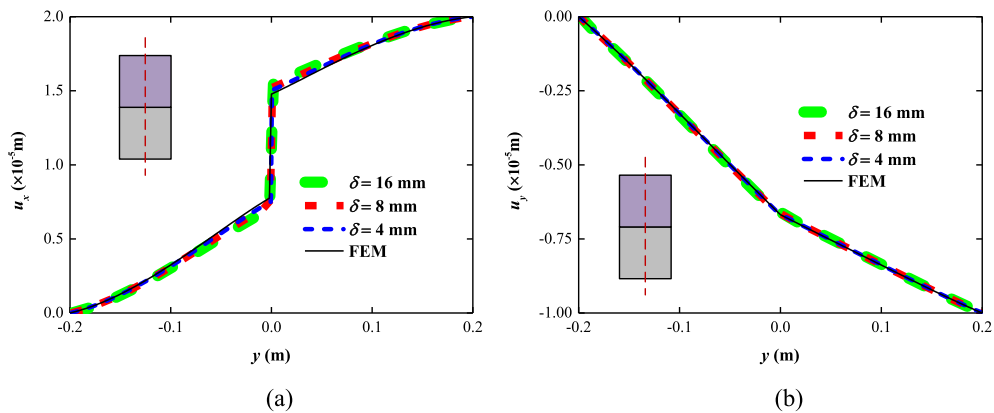


Fig. 9. Displacement distributions along the middle line in x-direction (a) and y-direction (b), when $u_x = 2.0 \times 10^{-5}$ m (sliding friction).

Table 2

Total contact forces of the contact surface.

δ (mm)	$u_x = 1.0 \times 10^{-5}$ m (surface sticking)				$u_x = 2.0 \times 10^{-5}$ m (sliding friction)			
	16	8	4	FEM	16	8	4	FEM
F_x (N)	-107.42	-104.68	-103.14	-101.11	-139.07	-136.58	-135.32	-134.76
F_y (N)	703.04	686.57	678.44	673.96	695.37	682.92	676.60	673.29

shown in Figs. 8 and 9, where the values of $\delta = 16$ mm, 8 mm and 4 mm, and the fixed value of $m = 4$ are utilized for the δ -convergence study. As shown in Figs. 6-9, for both $u_x = 1.0 \times 10^{-5}$ m and $u_x = 2.0 \times 10^{-5}$ m cases, the displacements from the present model greatly match those from the FEM results. Additionally, the solutions show that when $u_x = 1.0 \times 10^{-5}$ m, the displacements are continuous in the whole system and the contact surface is sticking; while when $u_x = 2.0 \times 10^{-5}$ m, the x-directional displacement is discontinuous across the contact surface (see Fig. 9(a)), and the sliding frictional contact is presented.

Furthermore, total contact forces of the contact surface are reported in Table. 2, in which different values of horizon δ are considered. As shown, in both $u_x = 1.0 \times 10^{-5}$ m (surface sticking) and $u_x = 2.0 \times 10^{-5}$ m (sliding friction) cases, the total contact forces predicted by peridynamics are converging to the FEM solutions as horizon sizes δ decrease, and the maximum differences of peridynamic results to FEM solutions are 2.0 % and 1.0 % for sticking and sliding frictional contact, respectively. Additionally, in the $u_x = 1.0 \times 10^{-5}$ m (sticking) case, the total tangential contact force F_x is smaller than 0.2 time of total normal contact force F_y , as $F_x < \mu F_y$; while in $u_x = 2.0 \times 10^{-5}$ m (sliding friction) case, $F_x = \mu F_y$ is satisfied.

4.1.2. Impact contact of two plates

Then, the impact contact of the two plates is investigated (see Fig. 10), in which the same geometrical sizes and material properties are utilized. The impact velocity of contactor $v_0 = 10$ m/s is considered. For the numerical simulation, the fixed mesh sizes of $\delta = 4$ mm and $m = 4$ are utilized. The explicit time integration scheme is performed, and the uniform time step of 3.0×10^{-8} s is used.

The total normal contact force during impact contact is presented in Fig. 11, in which different values of the modified coefficient β_n

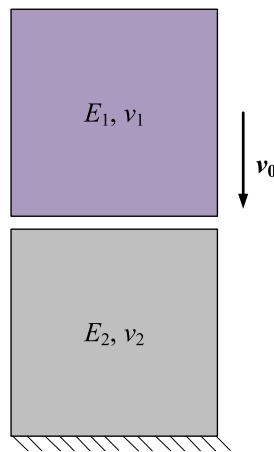


Fig. 10. Impact contact of two plates with different materials.

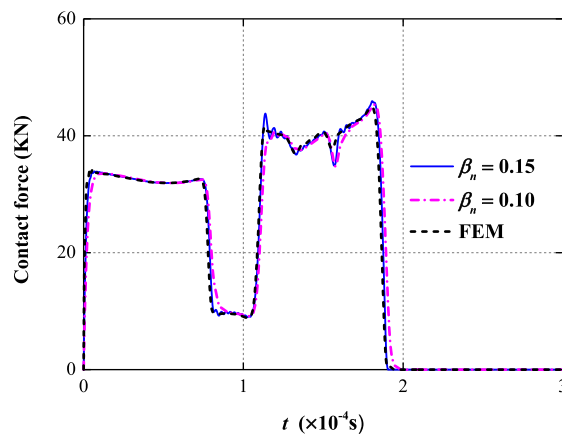


Fig. 11. Total normal contact force of the contactor during the impact test.

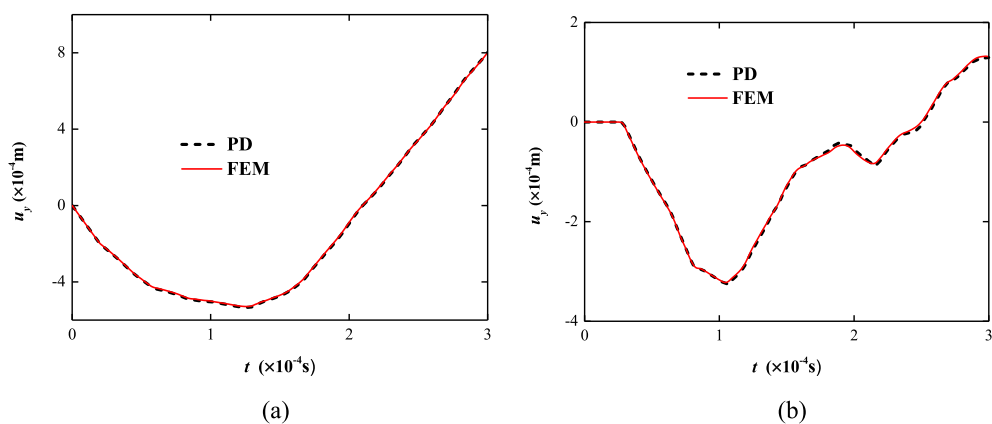


Fig. 12. Y-direction displacement of middle nodes in contactor (a) and target (b) plates during the impact test.

are considered. As shown in Fig. 11, the contact force increases rapidly at the beginning of contact, and finally decreases to zero at 1.9×10^{-4} s when the contact is released. Meanwhile, the total force predicted from peridynamic contact model has a nice coincidence with the FEM solution, though the numerical oscillations exist because of the explicit time integration scheme in this dynamic contact. According to the numerical tests, the oscillations can be largely reduced when the modified coefficient $\beta_n = 0.15$ is utilized, thus the

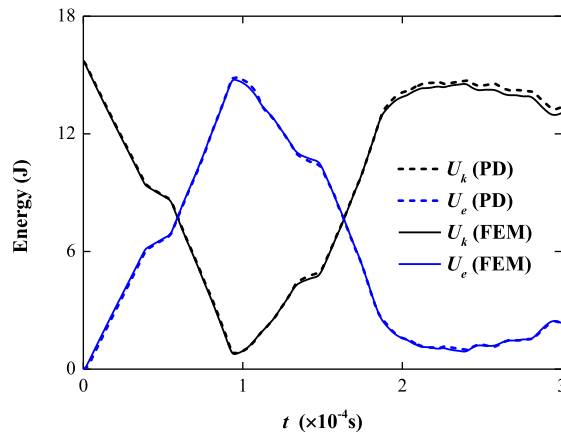


Fig. 13. The total kinetic energy (U_k) and elastic strain energy (U_e) of the whole system during the impact test.

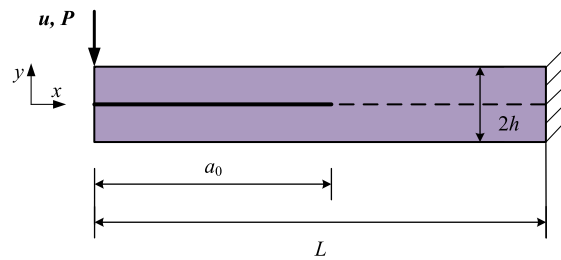


Fig. 14. End loaded split (ELS) test with a preset frictional crack along the middle interface.

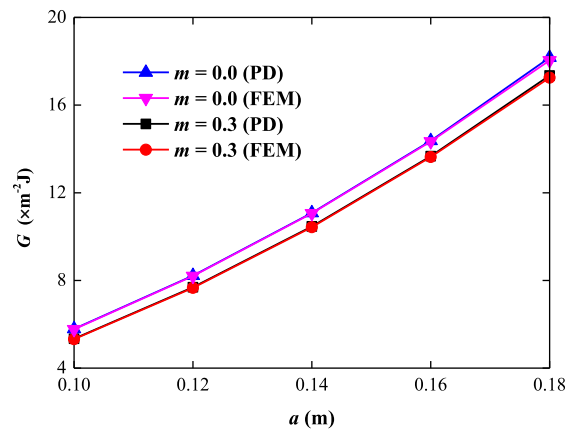


Fig. 15. Energy release rates of ELS specimens with different values of crack length a_0 .

reasonable value of modified coefficient $\beta_n = 0.15$ is considered in this dynamic contact problem.

Typically, the y -directional displacement of the middle nodes in contactor (upper) and target (down) plates during the impact are shown in Fig. 12. As shown, the middle node in the target plate starts to move downward due to the impact wave at 1.1×10^{-5} s, and keeps moving even when the contact is released at 1.9×10^{-4} s. Meanwhile, the total kinetic and elastic strain energies of the whole system are presented in Fig. 13. As shown in Fig. 13, the summation of the total kinetic and strain energy keeps in constant value of 15.7 J during the whole impact test, which is equal to the initial kinetic energy of the contactor with the velocity of 10 m/s.

In summary, the contact of two elastic plates are well predicted by the proposed peridynamic model, in which the sticking and sliding frictional contact are modeled, and the dynamic process of the impact contact is predicted.

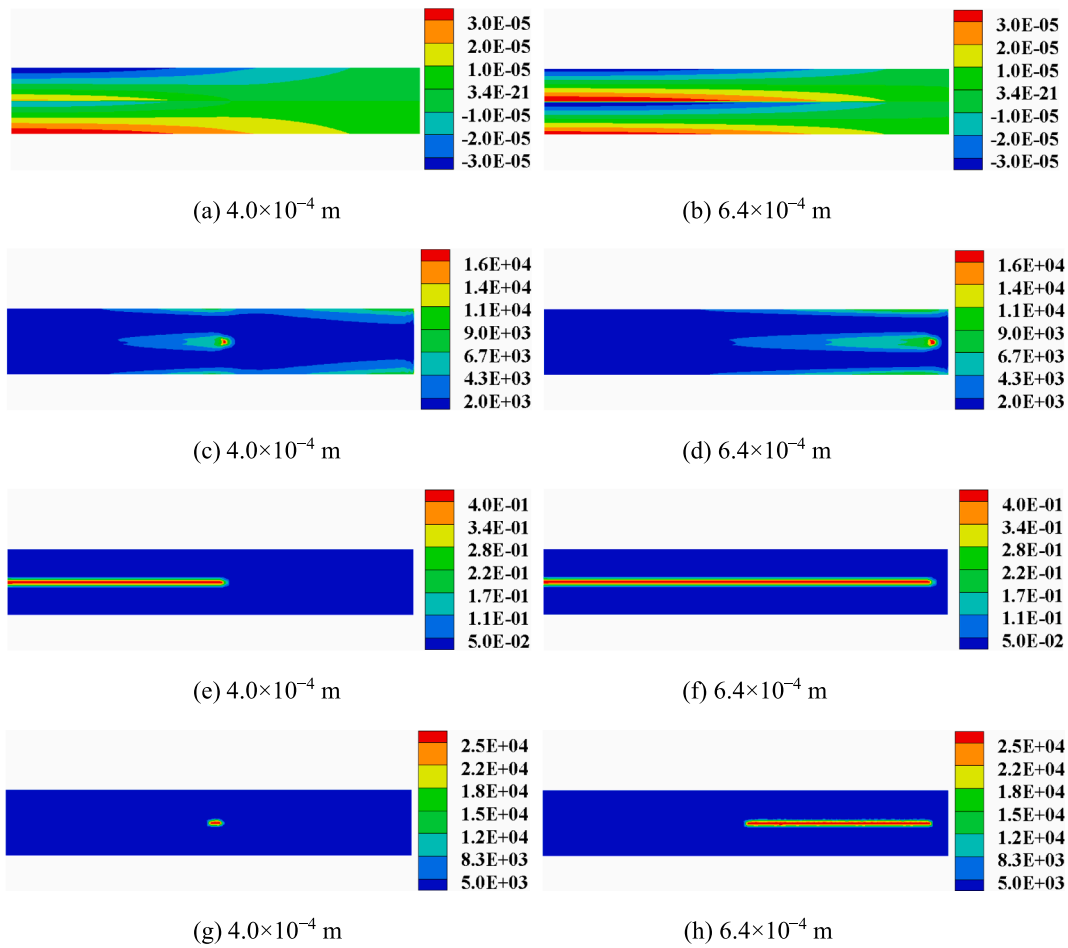


Fig. 16. Distributions of x -direction displacement (m) [(a) and (b)], strain energy density (J/m^3) [(c) and (d)], local damage/crack path [(e) and (f)], and released energy density (J/m^3) [(g) and (h)] of the ELS specimen under the displacement load of 4.0×10^{-4} m and 6.4×10^{-4} m.

4.2. Frictional fracture of end loaded split (ELS) test

The end loaded split (ELS) test [50], usually utilized for pure II interface delamination analysis, is then analyzed for contact investigation with frictional fracture. As shown in Fig. 14, the geometrical sizes of ELS specimen are given as: $L = 240$ mm and $h = 40$ mm. The plane stress condition is considered with the uniform thickness of 1 mm. The elastic isotropic material is utilized, and the material properties are: $E = 214$ GPa, $\nu = 0.3$ and $\rho = 7850$ kg/m².

A preset crack exists along the middle interface, the fracture toughness of $G_{IIc} = 100$ J/m² is used, and the frictional coefficient values of $\mu = 0.0$ and 0.3 are respectively considered. As the load is applied at the top of specimen (see Fig. 14), the frictional contact exists in the preset crack surface. In peridynamic numerical model, the fixed mesh sizes of $\delta = 4$ mm and $m = 4$ are used. The sliding frictional contact is considered with the peridynamic contact model of Eqs. (4) and (5), and the values of the contact horizon $\delta_c = 1.2\Delta x$ and the modified coefficient $\beta_n = 0.15$ are utilized.

4.2.1. Energy release rate of frictional crack

The energy release rate of the frictional crack is first analyzed, in which the fixed constant load of $P = 20$ N is considered (see Fig. 14). The PD_VCCT method [22] is utilized for the energy release rate computation in peridynamic model, and FEM-based VCCT method is used for the results comparison.

As shown in Fig. 15, the energy release rates of interface cracks with varying crack lengths a_0 are presented, in which different frictional coefficient values of $\mu = 0.0$ and 0.3 are considered. As shown in Fig. 15, the numerical energy release rates from peridynamic contact model closely match with FEM solutions within the maximum difference of 1.0%. Meanwhile, compared to the frictionless case ($\mu = 0.0$), the energy release rates of the frictional cracks ($\mu = 0.3$) decrease about 5%. Which means that the surface friction has a non-negligible influence on the crack energy release rate, and would further affect the fracture behaviors.

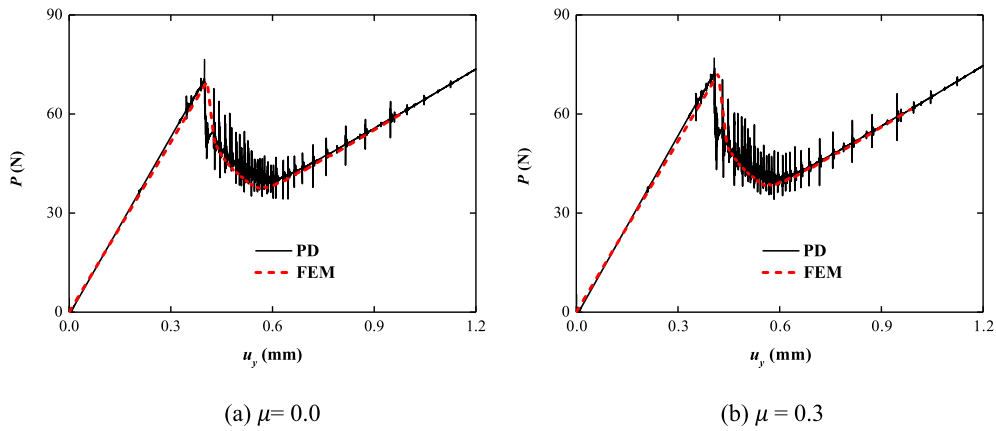


Fig. 17. Applied load versus displacement of ELS specimens with different values of frictional coefficient (a) $\mu = 0.0$ and (b) $\mu = 0.3$.

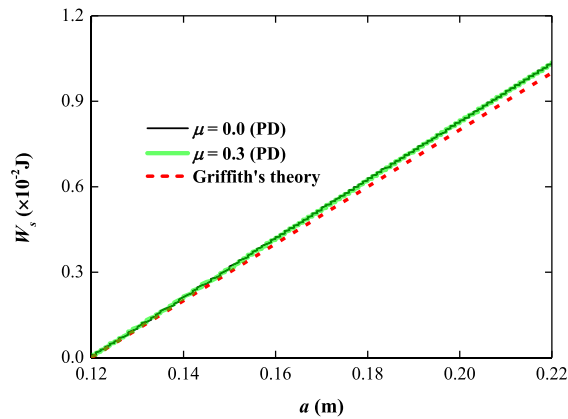


Fig. 18. Incremental surface energy related to crack length of ELS specimens with different frictional coefficients of (a) $\mu = 0.0$ and (b) $\mu = 0.3$.

4.2.2. Frictional interface fracture behaviors of ELS test

Then, the linearly increasing displacement of $u(t) = -2.0 \times 10^{-2} * t$ m is applied on the ELS specimen (see Fig. 14), and interface fracture behaviors with the frictional contact are investigated. For pure II fracture analysis, the angle-dependent critical stretch bond failure criterion in [15] is utilized. The explicit time integration scheme is performed, and uniform stable time step [51] is set as 3.0×10^{-8} s.

The distributions of x -direction displacement, strain energy density, local damage and released energy density of the ELS specimen under the displacement loads of 4.0×10^{-4} m and 6.4×10^{-4} m are presented in Fig. 16, where the pre-crack length $a_0 = 120$ mm and the frictional coefficient $\mu = 0.3$ are considered. Generally, under the y -directional displacement loading, the x -direction displacement distribution is antisymmetric (see Fig. 16(a) and (b)), the strain energy density distribution is symmetric (see Fig. 16(c) and (d)), with respect to the middle interface. It shows that the frictional crack tip is under pure II condition, and the top displacement loading is successfully transmitted to the bottom part through the surfaces contact. Meanwhile, with concentration of the strain energy density at the pre-crack tip (see Fig. 16(c)), the crack starts to grow around 2.0×10^{-2} s (see Fig. 16(e)) and propagates along the interface (see Fig. 16(f)). And the released energy density also appears with the crack growth by gathering all the broken bond energy (see Fig. 16(g) and (h)).

The applied load–displacement curves of ELS tests are shown in Fig. 17, where the different values of $\mu = 0.0$ and 0.3 are respectively utilized. Generally, the applied load first linearly increases with the linearly increasing displacement, and drops with numerical oscillations when the crack starts to grow. Compared to FEM solutions, the applied load–displacement relationships are successfully captured by peridynamic model in both $\mu = 0.0$ and $\mu = 0.3$ cases. Typically, the predicted critical loads of the ELS specimens are 70.7 N and 73.3 N for $\mu = 0.0$ and $\mu = 0.3$, respectively, within the maximum difference of 1.3 % to the FEM solutions (i. e. 69.9 N and 72.3 N). It also shows that the friction on the contact surface would increase the critical load of ELS specimen.

Additionally, the plots of the total released energy related to the crack length are given in Fig. 18. As presented, the curves for different frictional coefficients are nearly coincident, and they have the close slope to the Griffith's theory. The calculated energy release rate G_Q , which is defined in [13], is 96.3 J/m^2 and 96.2 J/m^2 for the cases of $\mu = 0.0$ and $\mu = 0.3$, with the differences of 3.7 % and 3.8 % to the input theoretical value (i.e. 100 J/m^2).

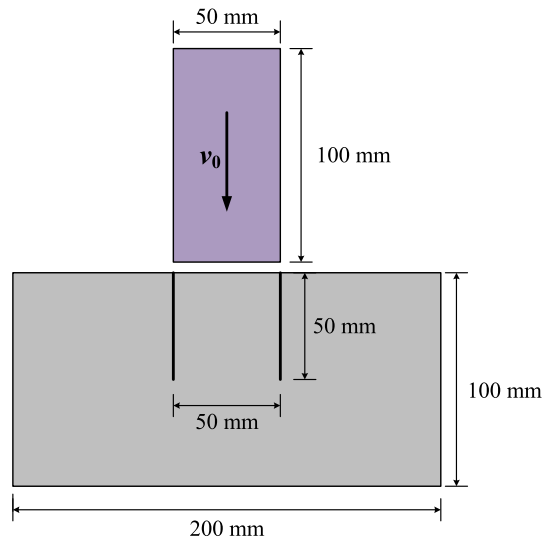


Fig. 19. Geometric sizes and impact condition of Kalthoff-Winkler test.

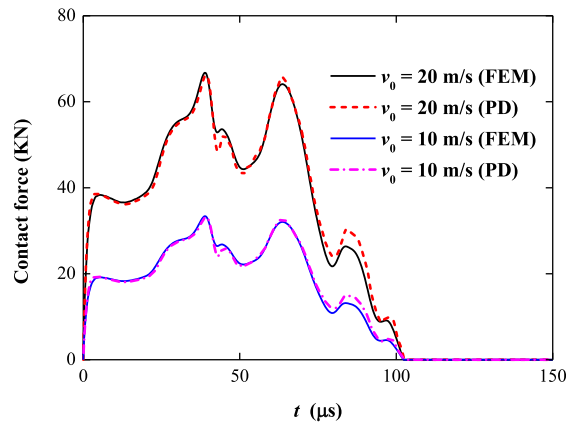


Fig. 20. Total contact normal forces during the impact tests with different impact velocity conditions.

Overall, the numerical results show that the proposed contact model can successfully capture the fracture behaviors of the ELS interface fracture, in which the frictional contact happens along the preset crack surfaces. And the friction effect on the contact surface would decrease the energy release rate and increase the critical load of ELS specimen.

4.3. Kalthoff-Winkler (KW) test

A plate with two edged notches impacted by a projectile, called as the Kalthoff-Winkler test [52], is presented in Fig. 19, which is a benchmark problem for dynamic fracture. The two-dimensional (2D) plane stress condition is considered, and the thickness of target plate is 1 mm; while the thickness of projectile block is set as 39.25 mm to ensure the block has the same cross section as the experimental cylinder. The elastic material in [53] is considered for both projectile block and target plate, and material properties are presented as: $E = 190$ GPa, $\nu = 0.3$, $\rho = 8000$ kg/m³ and $G_c = 2.217 \times 10^4$ J/m².

In the numerical peridynamic model, the fixed mesh sizes of $\delta = 4$ mm, 2 mm and $m = 4$ are utilized. The explicit time integration scheme is performed with the uniform time step of 1.0×10^{-8} s. The critical stretch bond failure criterion [15] is utilized for dynamic fracture analysis. And the contact horizon $\delta_c = 4\Delta x$ and the modified coefficient $\beta_n = 0.15$ are utilized for the contact analysis.

First, the impact response of target plate is investigated without crack growth, and total contact normal forces during the impact tests are presented in Fig. 20, in which different impact velocities of 10 m/s and 20 m/s are considered with the comparison to the FEM solutions. As shown in Fig. 20, the total contact forces of different impact velocities have the similar tendency, and they decrease to zero at 102.7 μ s when the contact is released. Meanwhile, the values of contact force are consistent to the FEM results for both $v_0 = 10$ m/s and $v_0 = 20$ m/s cases.

Then, the peridynamic bond failure criterion is applied for crack growth modeling in the KW impact test, and the crack paths of

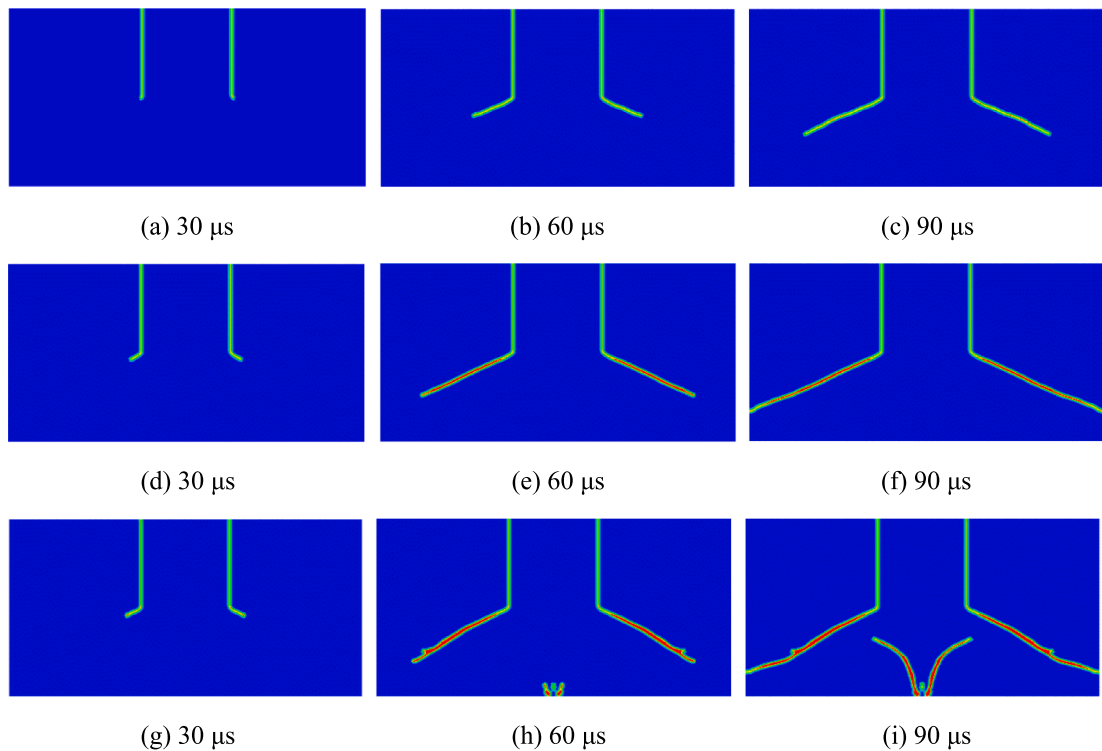


Fig. 21. Local damage (crack path) distributions during impact tests with the impact velocity of $v_0 = 10$ m/s [(a), (b) and (c)], $v_0 = 16.5$ m/s [(d), (e) and (f)], and $v_0 = 20$ m/s [(g), (h) and (i)].

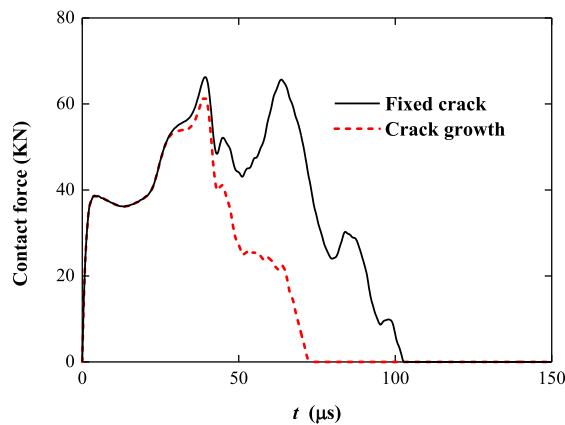


Fig. 22. Total contact normal forces during the KW impact tests with or without crack growth when impact velocity $v_0 = 20$ m/s.

impacted plates under different impact velocities are shown in Fig. 21. Generally, the cracks grow symmetrically by kinking an angle, about 68° respected to the initial crack direction, which greatly matches with the experimental observed angle of 70° [52]. Typically, as impact velocity $v_0 = 10$ m/s, the cracks start to grow at $28.4 \mu\text{s}$ and stop propagating at $101 \mu\text{s}$ with the final crack length of 52.5 mm; while as $v_0 = 16.5$ m/s, the cracks start to propagate at $23.3 \mu\text{s}$ and arrive to the boundary at $81.5 \mu\text{s}$, in which the crack path is nearly straight (see Fig. 21 (f)); when the value of v_0 increases to 20 m/s, the preset crack grows at $16.9 \mu\text{s}$, and two extra cracks initiate from the middle of bottom at around $60.0 \mu\text{s}$ (see Fig. 21 (h)) and propagate symmetrically toward the existed crack surface (see Fig. 21 (i)).

Additionally, total contact normal forces during the impact tests with or without crack growth are presented in Fig. 22. Compared to the fixed crack case, the contact force drops rapidly when crack starts to propagate, and decreases to zero at $73.4 \mu\text{s}$. It is because the internal energy of the impacted plate is released by the growing cracks. Meanwhile, the crack speeds during the KW tests are given in Fig. 23, in which the different horizon sizes of $\delta = 4$ mm and 2 mm, and the impact velocity $v_0 = 16.5$ m/s are considered. As shown in

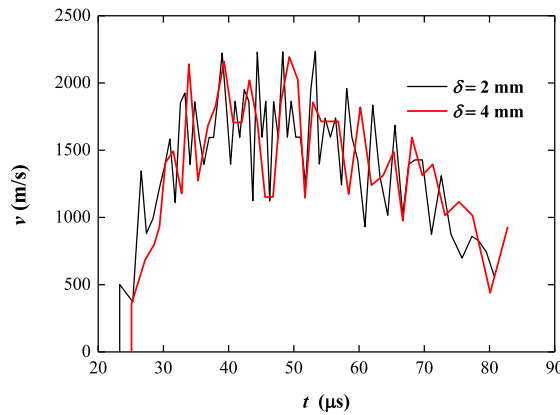


Fig. 23. Velocity of the crack tip with different mesh sizes when impact velocity $v_0 = 16.5$ m/s.

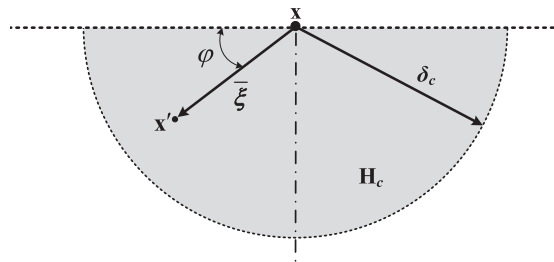


Fig. 24. A node to region contact model for contact bond micromodulus computation.

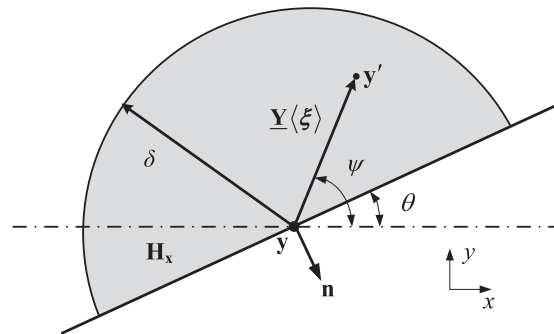


Fig. 25. The normal vector computation of boundary node in the deformed state.

Fig. 23, the crack speeds first increase, and then decrease at about $50 \mu\text{s}$. And the maximum crack speed is around 1700 m/s, about 61% of the Rayleigh wave speed, which is 2799.2 m/s based on its material properties.

In summary, the KW impact behavior is well predicted by the peridynamic model, in which the kinking angle, crack path and crack speed of the KW specimens are successfully captured.

5. Conclusions

In this paper, a new nonlocal peridynamic contact model is proposed for contact problems analysis. First, the long-range peridynamic contact bond forces are developed for sticking and sliding frictional contact, and the corresponding numerical algorithm is proposed for normal vector computation and contact condition evaluation. Then, three numerical examples, including contact of two plates, the end loaded split and Kalthoff-Winkler tests are studied to verify the proposed model.

As examples, the sticking, sliding frictional and impact contact of two elastic plates are well predicted by the proposed contact model, with a good agreement to the FEM solutions. The reasonable value of modified coefficient $\beta_n = 0.15$ is obtained in the dynamic impact contact based on numerical tests. In the ELS test, the interface crack energy release rates and displacement-load curves are well

captured in both the frictionless ($\mu = 0.0$) and frictional ($\mu = 0.3$) cases. And the friction on the contact surface would decrease the energy release rate and increase the critical load. While in the KW test, the cracks grow by kinking an angle, about 68° respected to the initial crack direction, and the maximum crack speed is around 1700 m/s, about 61% of the Rayleigh wave speed when the impact velocity $v_0 = 16.5$ m/s.

In general, the sticking, frictional sliding, impact contact and the involving fracture behaviors are all well modeled by the proposed peridynamic contact model, with which the peridynamic theory can be utilized for the materials and structures failure analysis including both contact and fracture.

We declare that we have no known competing financial interests or personal relationships that could have appeared to influence the work entitled “A peridynamic model for contact problems involving fracture”.

CRedit authorship contribution statement

Heng Zhang: Methodology, Investigation, Data curation, Writing - original draft. **Xiong Zhang:** Formal analysis, Writing - review & editing, Supervision, Funding acquisition. **Yan Liu:** Formal analysis, Validation.

Declaration of Competing Interest

The authors declare that they have no known competing financial interests or personal relationships that could have appeared to influence the work reported in this paper.

Acknowledgements

The financial supports from the National Natural Science Foundation of China (Nos. 12172192, 12102226) and the China Post-doctoral Science Foundation (No. 2021M691798) are gratefully acknowledged.

Appendix A

A.1. Peridynamic contact bond micromodulus

In the peridynamic contact model, a boundary node \mathbf{x} contacting to its contact region H_c is presented in Fig. 24. For the unit area ds of this contact surface, the contact force along its normal vector is:

$$f_n = p ds = 2 \int_{H_c} \mathbf{f}(\bar{\xi}) \cdot \mathbf{n} dV_{\mathbf{x}'} dV_{\mathbf{x}} \quad (20)$$

where p is the pressure on the contact surface, $\mathbf{f}(\bar{\xi})$ is the peridynamic contact force density of bond $\bar{\xi}$, H_c is the contact region which is the half circle when grid size converges to zero, and $dV_{\mathbf{x}'}$ and $dV_{\mathbf{x}}$ are volumes of nodes \mathbf{x}' and \mathbf{x} . The first multiplier of 2 is for double sides of the contact surface.

Here, a uniform normal compressive strain $\varepsilon_n = -\varepsilon_0$ is considered in the contact region, the total normal force in ds can thus be obtained as:

$$f_n = p_0 ds = E_c \varepsilon_0 ds \quad (21)$$

where E_c is the contact stiffness. In the sticking contact peridynamic model, considering the uniform strain, and using the sticking bond force in Eq. (3), the total normal force can also be computed as:

$$f_n = 2 \int_{H_c} \mathbf{f}_s(\bar{\xi}) \cdot \mathbf{n} dV_{\mathbf{x}'} dV_{\mathbf{x}} = 2 \int_{H_c} c_s \varepsilon_0 \cos^2 \varphi \underline{\omega} \sin \varphi dV_{\mathbf{x}'} dV_{\mathbf{x}} \quad (22)$$

When the influence function $\underline{\omega} = \delta_c / |\bar{\xi}|$ is used, the integration solution of Eq. (22) in two-dimension (2D) can then be expressed as:

$$f_n = \frac{4}{3} c_s \varepsilon_0 \delta_c^2 B dV_{\mathbf{x}} = \frac{4}{3} c_s \varepsilon_0 \delta_c^2 B ds h_2 \quad (23)$$

Considering Eqs. (21) and (23), the peridynamic sticking contact micromodulus can be obtained as:

$$c_s = \frac{3E_c}{4\delta_c^2 B h_2} \quad (24)$$

where δ_c is the contact horizon, B is the thickness of 2D model, h_2 is the grid size of the contactor peridynamic model, and E_c is contact stiffness that takes the form of:

$$\frac{2}{E_c} = \frac{1 - \nu_1^2}{E_1} + \frac{1 - \nu_2^2}{E_2} \tag{25}$$

where E_1 and E_2 are the elastic modulus, ν_1 and ν_2 are the Poisson's ratios of the contactor and target.

While in the sliding contact peridynamic model, considering the normal contact bond force in Eq. (4), the total normal force is:

$$f_n = 2 \int_{H_c} \mathbf{f}_n(\xi) \cdot \mathbf{n} dV_x = 2 \int_{H_c} c_n \varepsilon_0 \omega dV_x \tag{26}$$

When the influence function $\omega = \delta_c \sin\varphi/|\xi|$ is utilized, the Eq. (26) can be rewritten as:

$$f_n = 4c_n \varepsilon_0 \delta_c^2 B dV_x = 4c_n \varepsilon_0 \delta_c^2 B dsh_2 \tag{27}$$

Considering Eqs. (21) and (27), the peridynamic sliding contact micromodulus takes the form of:

$$c_n = \frac{E_c}{4\delta_c^2 B h_2} \tag{28}$$

Generally, the sticking and sliding bond micromodulus for the peridynamic contact are respectively expressed in Eqs. (24) and (28). However, in the discrete peridynamic models, the contact region H_c in Fig. 24 is smaller than the assumed half circle. Meanwhile, similar to the penalty contact model in the SPH [8] and FEM [54], the numerical disturbance would appear in the dynamic contact problem because of the explicit time integration scheme. Thus, for the more stable solution, the sticking and sliding contact micromodulus can be rewritten as:

$$c_s = \beta_s \frac{3E_c}{4\delta_c^2 B h_2}; \quad c_n = \beta_n \frac{E_c}{4\delta_c^2 B h_2} \tag{29}$$

where β_s and β_n are the modified coefficients. As expected, for the quasi-static contact problems, the given values of the modified coefficient have small effect on the final stable solution; while for dynamic problems, the contact force oscillation would occur if the relatively large value of modified coefficient is utilized, and the incorrect solution would appear with the small contact micromodulus. However, the suitable modified coefficient can be obtained with serial numerical tests, with which the numerical contact oscillation can be largely reduced.

A.2. Normal vectors of peridynamic boundary nodes

In the deformed state, a boundary node \mathbf{x} and its neighborhood node \mathbf{x}' moves to \mathbf{y} and \mathbf{y}' , respectively (see Fig. 25). Here, the weighted mass of the peridynamic node \mathbf{x} is defined as:

$$q = \rho \underline{\mathbf{y}} \cdot \underline{\mathbf{y}} = \int_{H_x} \rho(\underline{\mathbf{y}\mathbf{y}}) \langle \xi \rangle V_\xi \tag{30}$$

where ρ is the density of node \mathbf{x} , $\underline{\mathbf{y}}$ is the deformation scalar state computed as $|\underline{\mathbf{y}}|$. In the Cartesian coordinate system, the bond deformation scalar can be computed as:

$$\underline{\mathbf{y}} \langle \xi \rangle = \sqrt{\sum_{I=1,2,3} (y'_I - y_I)^2} \tag{31}$$

where y_I and y'_I are the I directional components of the deformed vectors \mathbf{y} and \mathbf{y}' , respectively.

The gradient of the weighted mass can be expressed as:

$$q_{,I} = \int_{H_x} \rho(\underline{\mathbf{y}\mathbf{y}}) \langle \xi \rangle_{,I} V_\xi \tag{32}$$

Substitute Eq. (31) into Eq. (32), and apply the differential operation, the Eq. (32) can be rewritten into:

$$q_{,I} = \int_{H_x} 2\rho(y'_I - y_I) V_\xi, \quad (I = 1, 2, 3) \tag{33}$$

In the 2D case of Fig. 25, consider the half circle horizon H_x and apply the integral operation in the cylindrical coordinate, the Eq. (33) can be computed as:

$$q_{,x} = -\frac{4}{3} \rho \delta^3 \sin\theta; \quad q_{,y} = \frac{4}{3} \rho \delta^3 \cos\theta \tag{34}$$

Thus, the unit outward normal vector of node \mathbf{x} can be obtained:

$$\mathbf{n} = \frac{q_{,I}}{|q_{,I}|} = \{\sin\theta, -\cos\theta\}, \quad (I = x, y) \tag{35}$$

which exactly matches with the surface direction in Fig. 25. Therefore, in the discrete peridynamic numerical model, based on Eq. (33), the unit outward normal vector of boundary node \mathbf{x}_i can be obtained by:

$$\mathbf{n}_i = -\frac{\sum_{m \in H_i} (y_{ml} - y_{il}) V_m}{\left| \sum_{m \in H_i} (y_{ml} - y_{il}) V_m \right|} \quad (36)$$

where y_{ml} means the I directional component of deformed vector \mathbf{y}_m , V_m is the volume of point \mathbf{x}_m .

References

- [1] Johnson KL. In: Contact Mechanics. Cambridge University Press; 1985.
- [2] Yang M, Kim KS. The behavior of subinterface cracks with crack-face contact. Eng Fract Mech 1993;44(1):155–65.
- [3] Sun CT, Qian W. A treatment of interfacial cracks in the presence of friction. Int J Fract 1998;94:371–82.
- [4] Hughes TJR, Taylor RL, Sackman JL, Curnier A, Kanoknukulchai W. A finite element method for a class of contact-impact problems. Comput Methods Appl Mech Eng 1976;8(3):249–76.
- [5] Chan SK, Tuba IS. A finite element method for contact problems of solid bodies-Part I. theory and validation. Int J Mech Sci 1971;13(7):615–25.
- [6] Bathe KJ, Chaudhary A. A solution method for planar and axisymmetric contact problems. Int J Numer Methods Eng 1985;21(1):65–88.
- [7] Huang P, Zhang X, Ma S, Huang X. Contact algorithms for the material point method in impact and penetration simulation. Int J Numer Methods Eng 2011;85(4):498–517.
- [8] Campbell J, Vignjevic R, Libersky L. A contact algorithm for smoothed particle hydrodynamics. Comput Methods Appl Mech Eng 2000;184(1):49–65.
- [9] Randles PW, Libersky LD. Smoothed particle hydrodynamics: Some recent improvements and applications. Comput Methods Appl Mech Eng 1996;139(1-4):375–408.
- [10] Silling SA. Reformulation of elasticity theory for discontinuities and long-range forces. J Mech Phys Solids 2000;48(1):175–209.
- [11] Silling SA, Askari E. A meshfree method based on the peridynamic model of solid mechanics. Comput Struct 2005;83(17-18):1526–35.
- [12] Silling SA, Epton M, Weckner O, Xu J, Askari E. Peridynamic states and constitutive modeling. J Elast 2007;88(2):151–84.
- [13] Zhang H, Qiao P. A state-based peridynamic model for quantitative fracture analysis. Int J Fract 2018;211(1-2):217–35.
- [14] Foster J, Silling SA, Chen W. An energy based failure criterion for use with peridynamic states. Int J Multiscale Comput Eng 2011;9(6):675–88.
- [15] Zhang H, Zhang X, Qiao P. A new peridynamic mixed-mode bond failure model for interface delamination and homogeneous materials fracture analysis. Comput Methods Appl Mech Eng 2021;379:113728.
- [16] Wang Y, Han F, Lubineau G. Strength-induced peridynamic modeling and simulation of fractures in brittle materials. Comput Methods Appl Mech Eng 2021;374:113558.
- [17] Zhang H, Qiao P, Lu L. Failure analysis of plates with singular and non-singular stress raisers by a coupled peridynamic model. Int J Mech Sci 2019;157-158:446–56.
- [18] Zhang H, Qiao P. A coupled peridynamic strength and fracture criterion for open-hole failure analysis of plates under tensile load. Eng Fract Mech 2018;204:103–18.
- [19] Hu W, Ha YD, Bobaru F, Silling SA. The formulation and computation of the nonlocal J-integral in bond-based peridynamics. Int J Fract 2012;176(2):195–206.
- [20] Stenström C, Eriksson K. The J-contour integral in peridynamics via displacements. Int J Fract 2019;216(2):173–83.
- [21] Zhang H, Qiao P. On the computation of energy release rates by a peridynamic virtual crack extension method. Comput Methods Appl Mech Eng 2020;363:112883.
- [22] Zhang H, Qiao P. Virtual crack closure technique in peridynamic theory. Comput Methods Appl Mech Eng 2020;372:113318.
- [23] Yang D, He X, Liu X, Deng Y, Huang X. A peridynamics-based cohesive zone model (PD-CZM) for predicting cohesive crack propagation. Int J Mech Sci 2020;184:105830.
- [24] Yang D, He X, Yi S, Liu X. An improved ordinary state-based peridynamic model for cohesive crack growth in quasi-brittle materials. Int J Mech Sci 2019;153-154:402–15.
- [25] Tong Y, Shen W, Shao J, Chen J. A new bond model in peridynamics theory for progressive failure in cohesive brittle materials. Eng Fract Mech 2020;223:106767.
- [26] Ha YD, Bobaru F. Characteristics of dynamic brittle fracture captured with peridynamics. Eng Fract Mech 2011;78(6):1156–68.
- [27] Ha YD, Bobaru F. Studies of dynamic crack propagation and crack branching with peridynamics. Int J Fract 2010;162(1-2):229–44.
- [28] Diehl P, Prudhomme S, Lévesque M. A review of benchmark experiments for the validation of peridynamics models. J Peridynamics Nonlocal Model 2019;1(1):14–35.
- [29] Hu W, Ha YD, Bobaru F. Peridynamic model for dynamic fracture in unidirectional fiber-reinforced composites. Comput Methods Appl Mech Eng 2012;217-220:247–61.
- [30] Hu Y, Madenci E. Bond-based peridynamic modeling of composite laminates with arbitrary fiber orientation and stacking sequence. Compos Struct 2016;153:139–75.
- [31] Zhang H, Qiao P. A state-based peridynamic model for quantitative elastic and fracture analysis of orthotropic materials. Eng Fract Mech 2019;206:147–71.
- [32] Gerstle W, Sau N, Silling S. Peridynamic modeling of concrete structures. Nucl Eng Des 2007;237(12-13):1250–8.
- [33] Yang D, Dong W, Liu X, Yi S, He X. Investigation on mode-I crack propagation in concrete using bond-based peridynamics with a new damage model. Eng Fract Mech 2018;199:567–81.
- [34] Gu X, Zhang Q, Huang D, Yv Y. Wave dispersion analysis and simulation method for concrete SHPB test in peridynamics. Eng Fract Mech 2016;160:124–37.
- [35] Zhang K, Ni T, Sarego G, Zaccariotto M, Zhu Q, Galvanetto U. Experimental and numerical fracture analysis of the plain and polyvinyl alcohol fiber-reinforced ultra-high-performance concrete structures. Theor Appl Fract Mech 2020;108:102566.
- [36] Zhou X, Wang Y, Qian Q. Numerical simulation of crack curving and branching in brittle materials under dynamic loads using the extended non-ordinary state-based peridynamics. Eur J Mech A/Solids 2016;60:277–99.
- [37] Wang Y, Zhou X, Shou Y. The modeling of crack propagation and coalescence in rocks under uniaxial compression using the novel conjugated bond-based peridynamics. Int J Mech Sci 2017;128-129:614–43.
- [38] Macek RW, Silling SA. Peridynamics via finite element analysis. Finite Elem Anal Des 2007;43(15):1169–78.
- [39] Littlewood DJ. Simulation of dynamic fracture using peridynamics, finite element modeling, and contact, ASME Int. Mech Eng Congr Expo Proc 2010;9:209–17.
- [40] Littlewood DJ. Roadmap for Peridynamic Software Implementation; 2015.
- [41] Madenci E, Oterkus E, editors. Peridynamic Theory and Its Applications. New York, NY: Springer New York; 2014.
- [42] Ye L, Wang C, Chang X, Zhang HY. Propeller-ice contact modeling with peridynamics. Ocean Eng 2017;139:54–64.
- [43] Rabczuk T, Ren H. A peridynamics formulation for quasi-static fracture and contact in rock. Eng Geol 2017;225:42–8.
- [44] Lee J, Liu W, Hong J-W. Impact fracture analysis enhanced by contact of peridynamic and finite element formulations. Int J Impact Eng 2016;87:108–19.
- [45] Kamensky D, Behzadinasab M, Foster JT, Bazilevs Y. Peridynamic modeling of frictional contact. J Peridynamics Nonlocal Model 2019;1(2):107–21.
- [46] Zhang Y, Qiao P. Peridynamic simulation of two-dimensional axisymmetric pull-out tests. Int J Solids Struct 2019;168:41–57.

- [47] Lu W, Oterkus S, Oterkus E. Peridynamic modelling of Hertzian indentation fracture. *Procedia Struct Integr* 2020;28:1559–71.
- [48] Bobaru F, Yang M, Alves LF, Silling SA, Askari E, Xu J. Convergence, adaptive refinement, and scaling in 1D peridynamics. *Int J Numer Methods Eng* 2009;77(6):852–77.
- [49] Kilic B, Madenci E. An adaptive dynamic relaxation method for quasi-static simulations using the peridynamic theory. *Theor Appl Fract Mech* 2010;53(3):194–204.
- [50] Wang H, Vu-Khanh T. Use of end-loaded-split (ELS) test to study stable fracture behaviour of composites under mode II loading. *Compos Struct* 1996;36(1-2):71–9.
- [51] Zhang H, Qiao P. A two-dimensional ordinary state-based peridynamic model for elastic and fracture analysis. *Eng Fract Mech* 2020;232:107040.
- [52] Joerg FK. Modes of dynamic shear failure in solids. *Int J Fract* 2000;101:1–31.
- [53] Belytschko T, Chen H, Xu J, Zi G. Dynamic crack propagation based on loss of hyperbolicity and a new discontinuous enrichment. *Int J Numer Methods Eng* 2003;58(12):1873–905.
- [54] Baek H, Park K. Cohesive frictional-contact model for dynamic fracture simulations under compression. *Int J Solids Struct* 2018;144-145:86–99.